

Cloud top height  
trends in the oxygen  
A-band

L. Lelli et al.

This discussion paper is/has been under review for the journal Atmospheric Chemistry and Physics (ACP). Please refer to the corresponding final paper in ACP if available.

# Trends in cloud top height from passive observations in the oxygen A-band

L. Lelli<sup>1</sup>, A. A. Kokhanovsky<sup>1,\*</sup>, V. V. Rozanov<sup>1</sup>, M. Vountas<sup>1</sup>, and J. P. Burrows<sup>1</sup>

<sup>1</sup>Institute of Environmental Physics and Remote Sensing, University of Bremen, Otto-Hahn-Allee 1, 28334 Bremen, Germany

\*now at: EUMETSAT, Eumetsat Allee 1, 64295 Darmstadt, Germany

Received: 21 October 2013 – Accepted: 21 November 2013 – Published: 2 December 2013

Correspondence to: L. Lelli (luca@iup.physik.uni-bremen.de)

Published by Copernicus Publications on behalf of the European Geosciences Union.

Title Page

Abstract

Introduction

Conclusions

References

Tables

Figures

⏪

⏩

◀

▶

Back

Close

Full Screen / Esc

Printer-friendly Version

Interactive Discussion



## Abstract

Measurements by the hyperspectral spectrometers GOME, SCIAMACHY, and GOME-2 are used to determine the rate of linear change (and trends) in cloud top height (CTH) in the period between June 1996 and May 2012. The retrievals are obtained from Top-Of-Atmosphere (TOA) backscattered solar light in the oxygen A-band using the Semi-Analytical Cloud Retrieval Algorithm SACURA. The physical framework relies on the asymptotic equations of radiative transfer, valid for optically thick clouds. Using linear least-squares techniques, a global trend of  $-1.78 \pm 2.14 \text{ m yr}^{-1}$  in deseasonalised CTH has been found, in the latitude belt within  $\pm 60^\circ$ , with diverging tendencies over land ( $+0.27 \pm 3.2 \text{ m yr}^{-1}$ ) and ocean ( $-2.51 \pm 2.8 \text{ m yr}^{-1}$ ). The El Niño-Southern Oscillation (ENSO), strongly coupled to CTH, forces clouds to lower altitudes. The global ENSO-corrected trend in CTH amounts to  $-0.49 \pm 2.22 \text{ m yr}^{-1}$ . At a global scale, no explicit regional pattern of statistically significant trends (at 95 % confidence level, estimated with bootstrap technique) have been found, which would be representative of typical natural synoptical features. One exception is North Africa, which exhibits the strongest upward trend in CTH sustained by an increasing trend in water vapor.

## 1 Introduction

Tropospheric clouds are main players in the Earth's climate system. Characterization of long-term global cloud properties (top and bottom height, optical thickness and albedo, effective radius of droplets) aims to support radiation budget assessments as well as trace gas retrievals, and analysis of cloud interactions with aerosol particles and gases in the atmosphere. The altitude of a cloud plays a cardinal role because clouds at different heights exert different feedbacks. High-altitude clouds absorb infrared radiation coming from lower atmosphere and radiate like blackbodies, thus they can warm the atmosphere trapping radiation. At the same time, their albedo is small because they are, in most cases, comparably thin. Conversely, low-altitude clouds only weakly shield in-

### Cloud top height trends in the oxygen A-band

L. Lelli et al.

Title Page

Abstract

Introduction

Conclusions

References

Tables

Figures

◀

▶

◀

▶

Back

Close

Full Screen / Esc

Printer-friendly Version

Interactive Discussion



## Cloud top height trends in the oxygen A-band

L. Lelli et al.

Title Page

Abstract

Introduction

Conclusions

References

Tables

Figures

◀

▶

◀

▶

Back

Close

Full Screen / Esc

Printer-friendly Version

Interactive Discussion



frared radiation emitted by atmospheric gases to the outer space and they are strongly reflecting objects, owing to their relatively high optical density. While the net effect of high clouds, when looking at the tropical belt, is to warm the climate system, whereas lower clouds cool the system (Loeb et al., 2012), this situation may change if considering the Northeast Pacific over a decadal time window. Evidence of a positive feedback by low-level clouds has been demonstrated (Clement et al., 2009). It is therefore likely that no general description is possible on a global scale and regional studies should be conducted instead.

Moreover, a critical aspect of any trend analysis is that, due to the limitation of a relatively short derived CTH time serie, no statistical significance may be found. Previous works do not provide clear indications. The analysis of the 7 yr GOME record (June 1996–May 2003) by Loyola et al. (2010) shows a change of  $-4.8 \text{ m yr}^{-1}$  for the latitudinal belt within  $\pm 60^\circ$ . Davies and Molloy (2012) reported a decreasing global trend of  $-40 \text{ m decade}^{-1}$ , as seen by MISR on the Terra platform. Evan and Norris (2012) showed that the previous results were affected by instrumental artifacts. Corrected MISR time series exhibit opposite tendency, that is an increase of  $+54 \text{ m decade}^{-1}$ , supported by a MODIS (on Terra) upward trend of  $+60.9 \text{ m decade}^{-1}$ . The considered record length amounts to 8 yr, from March 2003 throughout February 2010.

In the present study it has been attempted to extend the cloud records including measurements of the three sensors GOME, SCIAMACHY and GOME-2 (hereinafter termed GSG). Since the launch of GOME, back in 1995, more than 17 yr of data are now available and they form the observational basis of the present analysis (June 1996–May 2012).

The manuscript has the following structure. Section 2 describes how the monthly-sampled cloud record is calculated from measured radiances. Section 3 introduces the model used to derive the rate of linear change in cloud top height. Section 4 is devoted to the main results of the work. First, an analysis of ENSO as reflected in cloud properties is presented and trends in cloud top height are assessed. In the last

section, the findings are summarized also giving conclusions and outlook for future work.

## 2 Data and methods

The spaceborne nadir-viewing spectrometers Global Ozone Monitoring Experiment (GOME, Burrows et al., 1999), Scanning Imaging Absorption spectrometer for Atmospheric CHartography (SCIAMACHY, Bovensmann et al., 1999) and GOME-2 (Callies et al., 2000) measure solar backscattered light at a spectral resolution of 0.24–1.48 nm (see Table 1 for their characteristics). In particular, they cover the wavelength range 758–772 nm (at  $\approx 0.4$  nm resolution) where is situated one of the absorption bands of molecular oxygen, the O<sub>2</sub> A-band.

The A-band is exploited by the Semi-Analytical ClOud Retrieval Algorithm (SACURA) (Rozanov and Kokhanovsky, 2004) to generate cloud top height (CTH) records in the following way: given the local fractional cloud cover ( $f$ ) obtained from broadband Polarization Measuring Devices (PMD) measurements with the Optical Cloud Recognition Algorithm (OCRA) (Loyola and Ruppert, 1998), the sun-normalised Earthshine reflectances are weighted with the Independent Pixel Approximation (IPA) (Marshak et al., 1995). In this way, the measured scene reflectance  $R_{\text{mes}}$  is scaled to the cloud reflectance  $R_{\text{cl}}$  generated by a full cloudy ( $f = 1$ ) and a cloud-free ( $f = 0$ ) pixel with

$$R_{\text{mes}} = fR_{\text{cl}} + (1 - f)R_{\text{s}}. \quad (1)$$

The accuracy of Eq.(1) is given by Kokhanovsky et al. (2007). The clear-sky reflectance  $R_{\text{s}}$  is substituted by the Minimum Lambert-Equivalent Reflectivity (MLER) taken from the global database Tropospheric Emission Monitoring Internet Service (TEMIS) (Koelemeijer et al., 2003). The cloud optical thickness (COT) is retrieved in the continuum at 758 nm and used for the computation of the forward TOA cloud reflectance with asymptotic approximations of radiative transfer (Kokhanovsky and

### Cloud top height trends in the oxygen A-band

L. Lelli et al.

Title Page

Abstract

Introduction

Conclusions

References

Tables

Figures

◀

▶

◀

▶

Back

Close

Full Screen / Esc

Printer-friendly Version

Interactive Discussion



## Cloud top height trends in the oxygen A-band

L. Lelli et al.

Title Page

Abstract

Introduction

Conclusions

References

Tables

Figures

◀

▶

◀

▶

Back

Close

Full Screen / Esc

Printer-friendly Version

Interactive Discussion



Rozanov, 2004). Then, the minimal difference between  $R_{cl}$  and the forward spectrum (modeled with the analytical equations of radiative transfer) is iteratively looked for along the whole  $O_2$  A-band, at the nominal spectral sampling of the instruments. The distinctive feature of SACURA is the modeling of clouds as scattering layers instead of Lambertian reflectors (Koelemeijer et al., 2001), therefore radiative transfer throughout, above and below the clouds is taken into account. A comprehensive description of the algorithm can be found in Lelli et al. (2012, and references therein), where also accuracy, validation and selection criteria of CTH retrievals are given.

Cloud top height retrievals ( $b$ ) are firstly binned in 13 height layers ( $k$ ) (see Table 2 for the grid definition), projected onto a equidistant rectangular grid of  $0.5^\circ$  sided-cells at latitude ( $i$ ) and longitude ( $j$ ), counted-averaged over all altitudes (being  $c_k$  the retrieval counts at height bin  $k$ ) at month  $t$  and the CTH means  $h_t$  are computed with

$$h_t(i, j) = \frac{\sum_k c_{kt}(i, j) b_{kt}(i, j)}{\sum_k c_{kt}(i, j)}. \quad (2)$$

This formulation has been chosen for consistency with Evan and Norris (2012, Eq. 1). The values for  $h_t$  are plotted in Fig. 1 for global (top) and tropical (bottom plot) region. In both cases, the time series of the individual instruments exhibit in-phase seasonality for the respective overlapping months, whereas the relative offsets (top plot) cannot be explained by the mere diurnal cycle clouds have, owing to the different overpass time of the instruments which fly 1/2 h ahead of each other, GOME-2 crossing first the equator at 9.30 a.m. In case of multi-layered cloud systems it is expected that sensors with coarser footprints, such as GOME ( $320 \times 40 \text{ km}^2$ ), will observe more high clouds at the expenses of low clouds as compared to finer resolved sensors, such as SCIAMACHY ( $60 \times 40 \text{ km}^2$ ) and GOME-2 ( $80 \times 60 \text{ km}^2$ ). On a individual pixel scale, this effect can be seen in Lelli et al. (2012, Fig. 8, p. 1559), in which a GOME-derived CTH was co-located with a ground-based radar-derived CTH for a three-layer cloudy scene. GOME retrieved the height of the uppermost cloud layer. On larger time and spatial scales, this situation is depicted in Fig. 2, which shows retrieval counts  $c_k$  (normalised to the total

number of counts) as function of height bin  $k$ , for different instruments and for global (left) and tropical (mid plot) region. The right plot of Fig. 2 shows the count difference between GOME and SCIAMACHY in both global and tropical region. Especially in the tropics, where heterogeneity is frequent, GOME counts increase toward higher layers of the troposphere. These values can be devised as correction factors for the harmonisation of time series among the instruments, given that the same scene is sensed and no time lag occurs between different measurements. Therefore, in the current analysis, it is preferred to compute the CTH anomalies of Fig. 3 subtracting the climatological seasonal cycle for each instrument separately, in order to avoid the introduction of post-hoc artifacts in the record. While the CTH anomalies from GOME and SCIAMACHY are in almost perfect agreement, the transition between SCIAMACHY and GOME-2 records is not smooth. This is likely due to calibration issues in the first year of GOME-2 operation: a change in the PMD pixel definitions was devised in April 2008 (EUMETSAT, 2010), which is seen to impact cloud fraction  $f$  and the cloud reflection function  $R_{cl}$  of Eq. (1). Thus, for the ensuing analysis, the merged time serie has been joined in June 2003 (GOME/SCIAMACHY) and May 2008 (SCIAMACHY/GOME-2).

### 3 Trend model

The basic requirement for the application of linear least-square regression is that the variable of interest is not persistent (Wilks, 2011). Persistence is the tendency for a variable to remain similar in time and is measured as the degree of temporal autocorrelation  $r_p$ . The dataset of this study is sampled on a monthly basis, thus autocorrelation at lag  $p = 1$  reveals the degree of persistence that CTH has after one month. The upper plot of Fig. 4 shows the autocorrelation  $r_p$  of CTH anomalies up to 4 months lag, for global and tropical region. It can be seen that in both cases the altitude of clouds does not exhibit almost any persistence. That is, the actual anomaly is not affected by values leading by one month. Since characteristic time scales of clouds range from minutes for individual shallow cloud cumulus to many hours for large stratiform cloud systems,

## Cloud top height trends in the oxygen A-band

L. Lelli et al.

Title Page

Abstract

Introduction

Conclusions

References

Tables

Figures

◀

▶

◀

▶

Back

Close

Full Screen / Esc

Printer-friendly Version

Interactive Discussion



over a month their features are randomised by intervening winds and persistence is not found. Therefore methods for normally distributed (gaussian) variables can be applied, given that the dataset has been deseasonalised. In the lower plot of Fig. 4 the mapped CTH autocorrelation signal (not exceeding  $r_p = 0.13$  over the Pacific Ocean) resembles ENSO-related patterns, stretching across the globe over the Atlantic and the Indian Oceans.

The trend magnitude  $\beta$  is calculated, at latitude and longitude  $(i, j)$ , with

$$Y_t(i, j) = \alpha(i, j) + \beta(i, j) \cdot X_t + \epsilon_t(i, j) \quad t = 1, \dots, 192 \quad (3)$$

where  $Y_t$  are the CTH anomalies,  $X$  is the temporal variable sampled at monthly step  $t$ ,  $\alpha$  and  $\epsilon_t$  the offset and the random noise, respectively. Among the techniques for the estimation of confidence intervals of the trend magnitude  $\beta$ , the *bootstrap resampling* (Efron and Tibshirani, 1993) enables the treatment of potentially non-normal data without any assumption on the underlying probability distribution. It belongs to the group of nonparametric methods and the knowledge of the analytical form of the statistics is not required (Mudelsee, 2010). The guiding idea is the “plug-in” principle: a new scrambled dataset is drawn (resampling with replacement) from the original dataset and a new  $\beta'$  is calculated with Eq. (3). This procedure is repeated  $n$  times and an empirical sample distribution for  $\beta$  is estimated. This empirical distribution can be regarded as the approximated estimate to the unknown  $\beta$  distribution and  $\sigma_\beta$  can be associated with the random effects reflected in the data. The required confidence level is customary chosen as 95 %, implying a 2.5 % cutting-off probability level on either sides for a two-tailed distribution. When the probability density function of the unknown distribution is related to its standardised Gaussian approximation, the cutting-off level amounts to the mean value  $\approx 1.96$  standard deviations  $\sigma_\beta$  (Wilks, 2011, p.140). Therefore, at locations  $(i, j)$  where the ratio  $|\beta/\sigma_\beta| > 2$ , the trend magnitude  $\beta$  exceeds natural variability and is considered statistically significant.

Figure 5 shows the normalised probability density function (PDF) and the cumulative density function (CDF) of  $\beta$ , calculated with  $10^4$  bootstrap resamples, for global and

## Cloud top height trends in the oxygen A-band

L. Lelli et al.

Title Page

Abstract

Introduction

Conclusions

References

Tables

Figures

◀

▶

◀

▶

Back

Close

Full Screen / Esc

Printer-friendly Version

Interactive Discussion



tropical regions. The red tails of the PDF portray the confidence level calculated with the percentile method at 2.5 % and 97.5 % quantile and provide the estimate of the uncertainty associated with the trend value  $\beta$ .

## 4 Results

### 4.1 Cloud property changes coupling to ENSO

The El-Niño-Southern Oscillation (ENSO) has been recognized as the largest natural fluctuation that can establish teleconnections and modulate cloud properties. ENSO has to be understood as the tie between two different processes (Trenberth, 1997): the term *El Niño* is assigned to a yearly warming of the ocean current which streams along the coasts of Peru and Ecuador in late December. Regularly, but not every year, a more pronounced warming of the wide tropical-east pacific pool occurs, driven by the magnitude of trade wind flows. The atmospheric component of this perturbation is termed *Southern Oscillation*. The opposite phase, namely *La Niña*, corresponds to a cooling of the pacific basin. Quantitatively, ENSO is identified when SST gradient changes over the Central-East Pacific (170° W–120° W, 5° N–5° S) exceed  $\pm 0.5^\circ\text{C}$ , resulting in the standard Niño 3.4 climate index (US National Centers for Environmental Prediction (NCEP), 1993).

In Fig. 6 the Niño 3.4 index has been plotted together with the unsmoothed CTH and CF anomalies for the 17 yr of the GSG dataset and high ( $R = +0.77$ ) and moderate ( $R = +0.31$ ) correlations are observed for CTH and CF, respectively. It can also be noted that the maxima of the CF time serie are not in phase with the warm ENSO phases and are delayed by approximately 2 months. The CTH and CF anomaly time series have been partitioned for high clouds (defined as clouds with altitude  $h > 7$  km), middle clouds ( $3.2\text{ km} < h < 7$  km) and low clouds ( $h < 3.2$  km), smoothed with Bezier polynomials to increase readability and plotted in Fig. 7. The correlation coefficients (calculated with unsmoothed data) reported on the right clearly indicate that a warm (cold) ENSO phase

## Cloud top height trends in the oxygen A-band

L. Lelli et al.

Title Page

Abstract

Introduction

Conclusions

References

Tables

Figures



Back

Close

Full Screen / Esc

Printer-friendly Version

Interactive Discussion



corresponds to a decrease (increase) in CF for low ( $R = -0.55$ ) and mid ( $R = -0.31$ ) clouds, while high clouds increase (decrease) their coverage ( $R = +0.53$ ). In Fig. 7 it is also shown that the lagged extrema in CF of Fig. 6 originate in the lowest layers of the troposphere, because CF for low- and mid-level clouds always anticipate the extrema for high clouds.

More precisely, the coupling of CTH and CF to El Niño can be understood inspecting Fig. 8, where  $R$  for either cloud parameters has been plotted as function of altitude bin  $h$ . Starting from the Planet Boundary Layer (PBL) ( $h < 2$  km), a warmer ocean surface produces evaporation and CF increases ( $R = +0.39$ ), while CTH does not exhibit almost any correlation ( $R = -0.11$ ). Departing from the PBL ( $2 \text{ km} \leq h < 8$  km), the cloud field is compressed by winds (CF decreases in response to warming,  $-0.30 \leq R \leq -0.41$ ) and convection lifts clouds higher up (CTH increases in response to warming,  $+0.16 \leq R \leq +0.38$ ). Within the upper layer of the troposphere ( $h \geq 8$  km), clouds rise until the tropopause ( $h \approx 16\text{--}17$  km) stops their ascent ( $-0.11 \leq R \leq 0$ ) and, concurrently, extend (CF increases,  $+0.19 \leq R \leq +0.44$ ), following the divergent air flow toward zones of lower pressure. This is consistent with the picture of a reinforced meridional circulation which squeezes clouds at low altitudes, while high clouds spread out in the horizontal direction and air masses close the Hadley cell. In fact, positive correlations between CF, SST and surface convergence are found by Norris (2005) for the International Satellite Cloud Climatology Project (ISCCP) high cloud amount and the ground-based Extended Edited Cloud Report Archive (EECRA) high-cloud record, calculated over almost the same region. Conversely, the warm pool situated in the western tropical Pacific ( $30^\circ \text{N}\text{--}30^\circ \text{S}$  and  $100^\circ \text{E}\text{--}160^\circ \text{E}$ ) is characterized by the reversed situation: deep convective clouds occur during cold La Niña periods. Hence negative correlations between CF and SST are found (Norris, 2005; Marchand, 2013). This dipole-like ENSO influence on cloud properties can be seen in Fig. 9, where diagrams of COT-CTH are drawn for the strongest ENSO within the GSG record (i.e. El Niño April 1997–May 1998 and the ensuing La Niña June 1998–June 2001) over the Niño 3.4 index box and the tropical warm pool.

## Cloud top height trends in the oxygen A-band

L. Lelli et al.

Title Page

Abstract

Introduction

Conclusions

References

Tables

Figures

◀

▶

◀

▶

Back

Close

Full Screen / Esc

Printer-friendly Version

Interactive Discussion



## Cloud top height trends in the oxygen A-band

L. Lelli et al.

Title Page

Abstract

Introduction

Conclusions

References

Tables

Figures

◀

▶

◀

▶

Back

Close

Full Screen / Esc

Printer-friendly Version

Interactive Discussion



Bjerknes (1969) already pointed out how trade winds and sea surface temperature (SST) mutually strengthen for both ENSO phases. Interestingly, he also argued that the ocean response to a change of the wind circulation patterns during El Niño has a characteristic lag of 2 months (this mechanism is known as *Bjerknes feedback*), such as the lag seen in the CF anomaly time series of Figs. 6 and 7. It is suggestive to regard this similarity as the manifestation of a two-way coupling between cloud properties and sea surface temperature. However, the dynamical interpretation rather than the energetic interpretation is here preferred for two reasons: not only the curves and the correlations of Fig. 7 have been calculated for the narrow Niño 3.4 climate index box, located in the Central-East Pacific, where the effect of the weakening of the longitudinal Walker circulation (corresponding to the onset of teleconnections) is at its maximum, but also Dessler (2011) showed that cloud changes have a negligible impact on SST, due to heat storage capacity and heat transport of the ocean, which dominates the ENSO climate variability.

The relationship between CTH, CF and ENSO has been investigated by Erlykin and Wolfendale (2010). Through the analysis of the ISCCP cloud cover and top pressure, they assert that both ENSO phases and global Earth's low troposphere temperature are negatively correlated with low-cloud amount. Thus, in the periods influenced by warm El Niño, low clouds are lift higher up and are reclassified as mid-level clouds. The opposite holds true for periods driven by La Niña. Since the last decade is showing more frequently cold episodes (59 % vs. 41 % occurrence of warm phases, see also Loeb et al., 2012), it is reasonable to suppose that the ENSO pulls clouds down.

### 4.2 Trends in cloud top height

Fig. 10 supports the argument introduced in the previous section: the removal of ENSO (excluding any data within longitudes of 170° W and 120° W and latitudes of 5° N and 5° S) shifts the overall trend, calculated in the latitudinal belt  $\pm 60^\circ$  (in order to lessen the influence of ice-capped regions), from  $-30.26$  m to  $-8.33$  m over 17 yr.

## Cloud top height trends in the oxygen A-band

L. Lelli et al.

Title Page

Abstract

Introduction

Conclusions

References

Tables

Figures

◀

▶

◀

▶

Back

Close

Full Screen / Esc

Printer-friendly Version

Interactive Discussion

The time series has been broken up for underlying surface and a trend of  $-2.51 \text{ myr}^{-1}$  over ocean and  $+0.27 \text{ myr}^{-1}$  over land are identified (lower plot of Fig. 10). No exhaustive explanation can be found for this divergent land/water trend on a global scale, due to the complexity and variety of tropospheric processes influencing the clouds. On a global scale, such effects might average out and give rise to well-defined cloud changes. Even so, it was noted (Wagner et al., 2008) that CTH reacts in response to a change in near-surface temperature (ST). The authors analyzed 7.5 yr of GOME data and showed not only a strong positive correlation between CTH and ST, but also that ST changes are highest over land. Thus, at the simplest level, global patterns of ST might explain the informations concealed in the diverging land/ocean CTH trends.

The findings are summarised in Table 3 together with previous results from independent datasets. The reported values show discrepancies. Indeed, the length of datasets as well as the instrumental spatial resolution can alter the rate of linear change in CTH, because different cloud features are sensed, both in space and time. It must be also noted that retrieved cloud properties and, therefore, trends are affected by the choice of the spectral window used in the algorithms. IR-based algorithms are sensitive to cirrus clouds, whereas NIR-based algorithms, such as SACURA, are valid for thick clouds. Moreover, SACURA takes into account  $\text{O}_2$  absorption inside the clouds and the retrieved cloud height cannot be regarded as *effective*, since it will be closer to its geometrical top in the case of a single-layer cloud.

Figure 11 shows global maps of trend magnitude  $\beta$  and standard deviation  $\sigma_\beta$ , degraded to  $5^\circ$ -sided cell mesh for computational efficiency and smoothed with the 8 neighboring cells. The maps indicate that trend magnitudes are zonally partitioned. The strongest trends are found over North Africa and the Arabian subcontinent ( $> +45 \text{ myr}^{-1}$ ), Central Eastern Pacific ( $-30 \text{ myr}^{-1}$ ) and Indian Ocean ( $-15 \text{ myr}^{-1}$ ). Conversely, the mid-latitudes ( $60^\circ \text{ N}-30^\circ \text{ N}$  and  $30^\circ \text{ S}-60^\circ \text{ S}$ ) are homogeneously characterised by a slightly decreasing trend ( $-2 \text{ myr}^{-1}$  on average). Fig. 11 shows also that the trend variability follows the oceanic contours, being over water almost always greater than  $20 \text{ myr}^{-1}$  in the latitude belt  $\pm 30^\circ$  and smaller than  $15 \text{ myr}^{-1}$  otherwise.



**Cloud top height trends in the oxygen A-band**

L. Lelli et al.

[Title Page](#)[Abstract](#)[Introduction](#)[Conclusions](#)[References](#)[Tables](#)[Figures](#)[◀](#)[▶](#)[◀](#)[▶](#)[Back](#)[Close](#)[Full Screen / Esc](#)[Printer-friendly Version](#)[Interactive Discussion](#)

An explanation can be found in large-scale outflows of fine-mode soot particles, that are produced in the Indian subcontinent during biomass burning seasons and transported over R2 (but not over R1) by easterly winds during the winter phase of the Indian monsoon. Indeed, most of the decreasing trend in  $H_2O$  is seen during winter seasons (Fig. 13, bottom right), while almost no trend is seen in summer months (Fig. 13, bottom left). The absorption of solar radiation by soot gives rise to two competing effects. On one hand, soot warms the atmospheric column (Feingold, 2005) and may cause clouds to dry out (Ackerman et al., 2000). On the other hand, soot depletes the amount of radiation reaching the surface, exerting a negative radiative forcing (Nakajima and Schulz, 2009), and the amount of energy at disposal for evaporation is diminished.

## 5 Conclusions

For the first time, spaceborne passive measurements of the  $O_2$  A-band have been used to identify the rate of linear change (trend) in cloud top height anomalies for the period June 1996–May 2012. The instruments used in this work are hyperspectrally resolved spectrometers (i.e. GOME, SCIAMACHY and GOME-2), payloads of polar orbiting platforms which cross the Equator at mid morning (local time). In particular, it has been seen that the instrumental spatial resolution impacts the calculation of mean values of apparent cloud top height at a monthly sampling. Owing to the sensing time lag among the instruments, the anomaly time series have been calculated for each sensor separately, once the climatological mean state of the cloud property of interest has been subtracted. Given that cloud top height, at monthly sampling, does not exhibit any significant persistence in time, the rate of linear change has been calculated with linear regression methods. The estimation of the distribution of cloud top height trends with bootstrap technique enabled the computation of confidence intervals and, consequently, the assessment of statistical significance.

First, cloud top height and, to a minor extent, cloud cover have been found to be coupled to ENSO in a dipole-like fashion across the Pacific Ocean. Patterns of

## Cloud top height trends in the oxygen A-band

L. Lelli et al.

Title Page

Abstract

Introduction

Conclusions

References

Tables

Figures

◀

▶

◀

▶

Back

Close

Full Screen / Esc

Printer-friendly Version

Interactive Discussion



cloud top height autocorrelation of magnitude 0.12–0.13 (vanishing after approximately 6 months) are seen over the Central-East Pacific, Atlantic and Indian Oceans, resembling the large scale fluctuations induced by ENSO. Moreover, the hallmark of the cold tongue in the central eastern Pacific is correlated with the strongest decreasing trend in cloud top height. The anomaly time serie of Fig. 3 clearly exhibits two dips, centered at the beginning of year 2000 and 2011. They resemble La Niña's periodicity, pointing to the ENSO's role played in the overall decreasing trend in cloud top height.

Second, except for trends derived from the same instrument (i.e. GOME), the comparison with trends previously published in the literature displays differences, which cannot be easily understood within a single explanation. In the case of MODIS and MISR trends (Evan and Norris, 2012), one notes that those instruments not only differ in spatial sampling but also are sensitive to thin clouds, in both solid and liquid phase. These clouds cannot be detected with the hyperspectral sensors in the O<sub>2</sub> A-band used in this work. Thus, the biases shown in Table 3 might point to a recent increasing trend of thin, typically cirrus, clouds. This argument could be also substantiated by the moderate decreasing CTH trend seen in both hemispherical mid-latitudes: since there is evidence on the widening of the Hadley cell (Allen et al., 2012, and references therein), the poleward displacement of cloudiness (Eastman and Warren, 2013) and the concurrent upward shift of high clouds on a synoptic scale (inferred from modeling studies, Singh and O'Gorman, 2012), this picture would imply a systematic thermodynamic phase change in high clouds. As a consequence, a lower occurrence of warm (liquid) clouds in the upper atmospheric layers suggests a higher occurrence of cirrus clouds (undetectable with the O<sub>2</sub> A-band), with the net effect of lowering the mean columnar cloud top height, as seen in the current dataset.

An indirect aerosol effect also has been observed. Natural and anthropogenic soot particles have an impact on cloud top height, modulating insulation and water evaporation over the Indian Ocean. Subsequently, during the winter phase of the Indian Monsoon, transport of moist air masses over the arid Arabian Peninsula exerts a negative feedback and decreases statistical significance of clouds' vertical displacement. In

fact, this effect has been already seen over Europe during the economic, industrial and infrastructural adjustments following the fall of the East Bloc (Devasthale et al., 2005).

In general, the representativeness of every trend is affected by the record length under study. 17 yr of data still might not be enough to provide any decisive answer to current open questions involving clouds. Therefore, future planned Earth's observing missions, such as MetOp-B/C and Sentinel-5 precursor with their respective payloads GOME-2 and TROPOMI (Veefkind et al., 2012), will enable the extension of the existing cloud records until and beyond 2022, supporting attribution studies of cloud property changes to natural or human causes and assessments of the cloud feedback sign within the climate system.

*Acknowledgements.* The authors are grateful to D. Loyola and W. von Hoyningen-Huene for discussions related to cloud and aerosol remote sensing. We also acknowledge S. Noël for providing the water vapor dataset, H. Bovensmann for his expertise in instrumental radiometry and R. Hommel for suggestions on a draft version of the manuscript. A special thank goes to W. Lotz for sharing his serious programming knowledge, which enabled accurate number crunching. SCIAMACHY and GOME-2 radiances have been made available by the European Space Agency (ESA) and the European Organisation for the Exploitation of Meteorological Satellites (EUMETSAT), respectively. GOME radiances and cloud fraction data (for GOME and GOME-2) have been made available by the German Aerospace Center (DLR) and generated under the auspices of the O3MSAF project funded by EUMETSAT and national contributions. Generic Mapping Tools (GMT, Wessel and Smith (1998)) and Climate Data Operators (CDO, Schulzweida et al., 2012) were used for this work. L. Lelli was supported by the DLR Sentinel-5 precursor project (grant nr. 50EE1247).

## References

Ackerman, A. S., Toon, O. B., Stevens, D. E., Heymsfield, A. J., Ramanathan, V., and Welton, E. J.: Reduction of tropical cloudiness by Soot, *Science*, 288, 1042–1047, doi:10.1126/science.288.5468.1042, 2000. 31421

## Cloud top height trends in the oxygen A-band

L. Lelli et al.

Title Page

Abstract

Introduction

Conclusions

References

Tables

Figures



Back

Close

Full Screen / Esc

Printer-friendly Version

Interactive Discussion



## Cloud top height trends in the oxygen A-band

L. Lelli et al.

Title Page

Abstract

Introduction

Conclusions

References

Tables

Figures

◀

▶

◀

▶

Back

Close

Full Screen / Esc

Printer-friendly Version

Interactive Discussion



- Allen, R. J., Sherwood, S. C., Norris, J. R., and Zender, C. S.: Recent Northern Hemisphere tropical expansion primarily driven by black carbon and tropospheric ozone, *Nature*, 485, 350–354, doi:10.1038/nature11097, 2012. 31422
- 5 Bjerknes, J.: Atmospheric teleconnections from the equatorial Pacific, *Mon. Weather Rev.*, 97, 163–172, doi:10.1175/1520-0493(1969)097<0163:ATFTEP>2.3.CO;2, 1969. 31418
- Bovensmann, H., Burrows, J. P., Buchwitz, M., Frerick, J., Noël, S., Rozanov, V. V., Chance, K. V., and Goede, A. P. H.: SCIAMACHY: mission objectives and measurement modes, *J. Atmos. Sci.*, 56, 127–150, doi:10.1175/1520-0469(1999)056<0127:SMOAMM>2.0.CO;2, 1999. 31412
- 10 Burrows, J. P., Weber, M., Buchwitz, M., Rozanov, V. V., Ladstättter Weissenmayer, A., Richter, A., DeBeek, R., Hoogen, R., Bramstedt, K., Eichmann, K. U., Eisinger, M., and Perner, D.: The Global Ozone Monitoring Experiment (GOME): mission concept and first scientific results, *J. Atmos. Sci.*, 56, 151–175, doi:10.1175/1520-0469, 1999. 31412
- 15 Callies, J., Corpaccioli, E., Eisinger, M., Hahne, A., and Lefebvre, A.: GOME-2-Metop's second-generation sensor for operational ozone monitoring, *ESA Bull.-Eur. Space*, 102, 28–36, 2000. 31412
- Clement, A. C., Burgman, R., and Norris, J. R.: Observational and model evidence for positive low-level cloud feedback, *Science*, 325, 460–464, doi:10.1126/science.1171255, 2009. 31411
- 20 Davies, R. and Molloy, M.: Global cloud height fluctuations measured by MISR on Terra from 2000 to 2010, *Geophys. Res. Lett.*, 39, L03701, doi:10.1029/2011GL050506, 2012. 31411, 31430
- Dessler, A. E.: Cloud variations and the Earth's energy budget, *Geophys. Res. Lett.*, 38, L19701, doi:10.1029/2011GL049236, 2011. 31418
- 25 Devasthale, A., Kruger, O., and Graßl, H.: Change in cloud-top temperatures over Europe, *IEEE Geosci. Remote S.*, 2, 333–336, 2005. 31423
- Eastman, R. and Warren, S. G.: A 39-yr survey of cloud changes from land stations worldwide 1971–2009: long-term trends, relation to aerosols, and expansion of the Tropical Belt, *J. Climate*, 26, 1286–1303, doi:10.1175/JCLI-D-12-00280.1, 2013. 31422
- 30 Efron, B. and Tibshirani, R. J.: *An Introduction to the Bootstrap*, Chapman and Hall, New York, 1993. 31415
- Erylkin, A. D. and Wolfendale, A. W.: Global cloud cover and the Earth's mean surface temperature, *Surv. Geophys.*, 31, 399–408, doi:10.1007/s10712-010-9098-7, 2010. 31418

## Cloud top height trends in the oxygen A-band

L. Lelli et al.

Title Page

Abstract

Introduction

Conclusions

References

Tables

Figures

◀

▶

◀

▶

Back

Close

Full Screen / Esc

Printer-friendly Version

Interactive Discussion



- EUMETSAT: GOME-2 PMD Band Definitions 3.0 and PMD Calibration, Tech. Rep. EUM/OPS-EPS/DOC/07/0601, EUMETSAT, Darmstadt, Germany, 2010. 31414
- Evan, A. T. and Norris, J. R.: On global changes in effective cloud height, *Geophys. Res. Lett.*, 39, L19710, doi:10.1029/2012GL053171, 2012. 31411, 31413, 31422, 31430
- 5 Feingold, G.: On smoke suppression of clouds in Amazonia, *Geophys. Res. Lett.*, 32, L02804, doi:10.1029/2004GL021369, 2005. 31421
- Koelemeijer, R. B. A., Stammes, P., Hovenier, J. W., and de Haan, J. F.: A fast method for retrieval of cloud parameters using oxygen A band measurements from the Global Ozone Monitoring Experiment, *J. Geophys. Res.*, 106, 3475–3490, doi:10.1029/2000JD900657, 2001. 10 31413
- Koelemeijer, R. B. A., de Haan, J. F., and Stammes, P.: A database of spectral surface reflectivity in the range 335–772 nm derived from 5.5 years of 0.5 observations, *J. Geophys. Res.*, 108, 4070, doi:10.1029/2002JD002429, available at: <http://www.temis.nl/data/ler.html> (last access: 11 October 2010), 2003. 31412
- 15 Kokhanovsky, A. A. and Rozanov, V. V.: The physical parameterization of the top-of-atmosphere reflection function for a cloudy atmosphere–underlying surface system: the oxygen A-band case study, *J. Quant. Spectrosc. Ra.*, 85, 35–55, doi:10.1016/S0022-4073(03)00193-6, 2004. 31412
- Kokhanovsky, A. A., Mayer, B., Rozanov, V. V., Wapler, K., Burrows, J. P., and Schumann, U.: The influence of broken cloudiness on cloud top height retrievals using nadir observations of backscattered solar radiation in the oxygen A-band, *J. Quant. Spectrosc. Ra.*, 103, 460–477, doi:10.1016/j.jqsrt.2006.06.003, 2007. 31412
- 20 Lelli, L., Kokhanovsky, A. A., Rozanov, V. V., Vountas, M., Sayer, A. M., and Burrows, J. P.: Seven years of global retrieval of cloud properties using space-borne data of GOME, *Atmos. Meas. Tech.*, 5, 1551–1570, doi:10.5194/amt-5-1551-2012, 2012. 31413
- 25 Loeb, N. G., Kato, S., Su, W., Wong, T., Rose, F. G., Doelling, D. R., Norris, J. R., and Huang, X.: Advances in understanding top-of-atmosphere radiation variability from satellite observations, *Surv. Geophys.*, 33, 359–385, doi:10.1007/s10712-012-9175-1, 2012. 31411, 31418
- Loyola, D. G. and Ruppert, T.: A new PMD cloud-recognition algorithm for GOME, *ESA Earth Obs. Quart.*, 58, 45–47, 1998. 31412
- 30 Loyola, D. G., Thomas, W., Spurr, R., and Mayer, B.: Global patterns in daytime cloud properties derived from GOME backscatter UV-VIS measurements, *Int. J. Remote Sens.*, 31, 4295–4318, doi:10.1080/01431160903246741, 2010. 31411, 31430

## Cloud top height trends in the oxygen A-band

L. Lelli et al.

Title Page

Abstract

Introduction

Conclusions

References

Tables

Figures

◀

▶

◀

▶

Back

Close

Full Screen / Esc

Printer-friendly Version

Interactive Discussion



- Marchand, R.: Trends in ISCCP, MISR, and MODIS cloud-top-height and optical-depth histograms, *J. Geophys. Res.-Atmos.*, 118, 1941–1949, doi:10.1002/jgrd.50207, 2013. 31417, 31420
- 5 Marshak, A., Davis, A., Wiscombe, W., and Titov, G.: The verisimilitude of the independent pixel approximation used in cloud remote sensing, *Remote Sens. Environ.*, 52, 72–78, doi:10.1016/0034-4257(95)00016-T, 1995. 31412
- Mieruch, S., Noël, S., Bovensmann, H., and Burrows, J. P.: Analysis of global water vapour trends from satellite measurements in the visible spectral range, *Atmos. Chem. Phys.*, 8, 491–504, doi:10.5194/acp-8-491-2008, 2008. 31420
- 10 Mudelsee, M.: *Climate Time Series Analysis: Classical Statistical and Bootstrap Methods*, Atmospheric and Oceanographic Sciences Library, vol. 42, Springer, Dordrecht, Heidelberg, London, New York, doi:10.1007/978-90-481-9482-7, 2010. 31415
- Nakajima, T. and Schulz, M.: What do we know about large-scale changes of aerosols, clouds, and the radiation budget?, in: *Clouds in the Perturbed Climate System*, edited by Heintzenberg, J. and Charlson, R. J., Strüngmann Forum Reports, 401–432, MIT Press, Cambridge, Massachusetts, 2009. 31421
- 15 Norris, J. R.: Trends in upper-level cloud cover and surface divergence over the tropical Indo-Pacific Ocean between 1952 and 1997, *J. Geophys. Res.*, 110, D21110, doi:10.1029/2005JD006183, 2005. 31417
- 20 Rozanov, V. V. and Kokhanovsky, A. A.: Semianalytical cloud retrieval algorithm as applied to the cloud top altitude and the cloud geometrical thickness determination from top-of-atmosphere reflectance measurements in the oxygen A band, *J. Geophys. Res.*, 109, 4070, doi:10.1029/2003JD004104, 2004. 31412
- Schulzweida, U., Müller, R., Kornblüh, L., Ansonge, C., and Quast, R.: CDO – Climate Data Operators – v1.5.9, Center for Marine and Atmospheric Sciences (ZMAW), Max-Planck Institute for Meteorology, University of Hamburg, available at: <https://code.zmaw.de/projects/cdo> (last access: 7 January 2013), 2012. 31423
- 25 Singh, M. S. and O’Gorman, P. A.: Upward shift of the atmospheric general circulation under global warming: theory and simulations, *J. Climate*, 25, 8259–8276, doi:10.1175/JCLI-D-11-00699.1, 2012. 31422
- 30 Trenberth, K. E.: The definition of El Niño, *B. Am. Meteorol. Soc.*, 78, 2771–2777, doi:10.1175/1520-0477(1997)078<2771:TDOENO>2.0.CO;2, 1997. 31416

## Cloud top height trends in the oxygen A-band

L. Lelli et al.

Title Page

Abstract

Introduction

Conclusions

References

Tables

Figures

◀

▶

◀

▶

Back

Close

Full Screen / Esc

Printer-friendly Version

Interactive Discussion



- US National Centers for Environmental Prediction (NCEP): Oceanic Niño Index (ONI), National Oceanic and Atmospheric Administration (NOAA), available at: <http://www.cpc.ncep.noaa.gov/products/precip/CWlink/MJO/enso.shtml>, (last access: 7 February 2013), 1993. 31416
- 5 Veefkind, J. P., Aben, I., McMullan, K., Förster, H., de Vries, J., Otter, G., Claas, J., Eskes, H. J., de Haan, J. F., Kleipool, Q., Van Weele, M., Hasekamp, O., Hoogeveen, R., Landgraf, J., Snel, R., Tol, P., Ingmann, P., Voors, R., Kruizinga, B., Vink, R., Visser, H., and Levelt, P. F.: TROPOMI on the ESA Sentinel-5 Precursor: A GMES mission for global observations of the atmospheric composition for climate, air quality and ozone layer applications, *Remote Sens. Environ.*, 120, 70–83, doi:10.1016/j.rse.2011.09.027, 2012. 31423
- 10 Wagner, T., Beirle, S., Deutschmann, T., Grzegorski, M., and Platt, U.: Dependence of cloud properties derived from spectrally resolved visible satellite observations on surface temperature, *Atmos. Chem. Phys.*, 8, 2299–2312, doi:10.5194/acp-8-2299-2008, 2008. 31419
- Wessel, P. and Smith, W. H. F.: New, improved version of Generic Mapping Tools (GMT) released, *EOS T. Am. Geophys. Un.*, 79, 579–579, doi:10.1029/98EO00426, 1998. 31423
- 15 Wilks, D. S.: *Statistical Methods in the Atmospheric Sciences*, vol. 100, 3rd edn, International Geophysics, Academic Press, New York, 2011. 31414, 31415

## Cloud top height trends in the oxygen A-band

L. Lelli et al.

**Table 1.** Technical specifications of the instruments used in this work. The bottom part of the table describes the Polarization Measuring Devices (PMD).

	GOME	SCIAMACHY	GOME-2
Data availability	1996–2011	2002–2012	2007–2022
Equator crossing (LT)	10.30 a.m.	10 a.m.	9.30 a.m.
Global coverage [days]	3	6	1.5
Spectral coverage [nm]	237–794	240–2400	237–794
Spectral resolution [nm]	0.38	0.44	0.48
Viewing geometry	nadir	nadir, limb, occultation	nadir
Ground pixel size [km <sup>2</sup> ]	320 × 40	60 × 40	80 × 60
Swath width [km]	≈ 960	≈ 1000	≈ 1920
Polarization	3p	6p	12 (s, p)
Spectral resolution [nm]	100–160	55–120	2.8–40
Spatial resolution [km <sup>2</sup> ]	40 × 20	30 × 7.5	40 × 5

Title Page

Abstract

Introduction

Conclusions

References

Tables

Figures

◀

▶

◀

▶

Back

Close

Full Screen / Esc

Printer-friendly Version

Interactive Discussion



## Cloud top height trends in the oxygen A-band

L. Lelli et al.

Title Page

Abstract

Introduction

Conclusions

References

Tables

Figures



Back

Close

Full Screen / Esc

Printer-friendly Version

Interactive Discussion



**Table 2.** Description of the height grid for calculation and analysis of cloud top height time series.

Cloud type	Height range [km]	Bins
Low	0–3.2	1–1.5 km, 1.5–2 km, 2–2.5 km, 2.5–3.2 km
Middle	3.2–7	3.2–5 km, 5–7 km
High	7–17	7–9 km, 9–11 km, 11–13 km, 13–15 km, 15–17 km

## Cloud top height trends in the oxygen A-band

L. Lelli et al.

**Table 3.** Overview of trends in cloud height [ $\text{mdecade}^{-1}$ ]<sup>a</sup>. Trends derived from the GSG dataset are given with (left column) and without (right column) ENSO, that has been filtered masking any data within the Niño 3.4 climate index box  $170^{\circ}\text{W}$ – $120^{\circ}\text{W}$ ,  $5^{\circ}\text{N}$ – $5^{\circ}\text{S}$

Base period [ $\text{year month}^{-1}$ ]	MISR	MISR corr.	MODIS	GOME	GSG	
03/03 – 11/02	–40.1 <sup>b</sup>	+54.3 <sup>c</sup>	+60.9 <sup>c</sup>	–	–10.7	+8.4
96/06 – 03/05	–	–	–	–47.9 <sup>d,e</sup>	–67.2 <sup>e</sup>	+25.2 <sup>e</sup>
96/06 – 12/05	–	–	–	–	–17.8	–4.9

<sup>a</sup> The GSG trends are recalculated for the length of the referenced dataset and latitude belt  $\pm 60^{\circ}$ .

<sup>b</sup> Davies and Molloy (2012).

<sup>c</sup> Evan and Norris (2012).

<sup>d</sup> Loyola et al. (2010).

<sup>e</sup> Extrapolated to decade.

Title Page

Abstract

Introduction

Conclusions

References

Tables

Figures

◀

▶

◀

▶

Back

Close

Full Screen / Esc

Printer-friendly Version

Interactive Discussion



## Cloud top height trends in the oxygen A-band

L. Lelli et al.

**Table 4.** Overview of zonal trends in cloud top height [ $\text{m yr}^{-1}$ ]. ENSO excluded masking any data within the box  $170^\circ \text{W}$ – $120^\circ \text{W}$ ,  $5^\circ \text{N}$ – $5^\circ \text{S}$ . Bootstrap resamples  $n = 10^3$ . The zonal values are not weighted by the respective land and water abundances.

	Belt		Land + Water	Land	Water
With ENSO	Tropics	$5^\circ \text{N}$ – $5^\circ \text{S}$	$-4.34 \pm 5.65$	$-1.56 \pm 4.02$	$-5.15 \pm 8.21$
		$20^\circ \text{N}$ – $20^\circ \text{S}$	$-2.16 \pm 2.97$	$1.83 \pm 4.40$	$-3.39 \pm 5.32$
	Mid latitude	$30^\circ \text{N}$ – $60^\circ \text{N}$	$-2.17 \pm 1.52$	$-2.85 \pm 4.23$	$-1.52 \pm 3.68$
		$30^\circ \text{S}$ – $60^\circ \text{S}$	$-2.71 \pm 2.59$	$-2.70 \pm 9.25$	$-2.71 \pm 2.47$
Without ENSO	Tropics	$5^\circ \text{N}$ – $5^\circ \text{S}$	$-1.80 \pm 6.00$	$-1.43 \pm 5.05$	$-1.99 \pm 8.52$
		$20^\circ \text{N}$ – $20^\circ \text{S}$	$0.53 \pm 3.53$	$5.93 \pm 5.33$	$-1.74 \pm 4.36$
	Mid latitude	$30^\circ \text{N}$ – $60^\circ \text{N}$	$-2.11 \pm 3.09$	$-2.72 \pm 4.60$	$-1.53 \pm 3.70$
		$30^\circ \text{S}$ – $60^\circ \text{S}$	$-2.78 \pm 2.54$	$-3.24 \pm 8.77$	$-2.75 \pm 2.35$

[Title Page](#)
[Abstract](#)
[Introduction](#)
[Conclusions](#)
[References](#)
[Tables](#)
[Figures](#)
[◀](#)
[▶](#)
[◀](#)
[▶](#)
[Back](#)
[Close](#)
[Full Screen / Esc](#)
[Printer-friendly Version](#)
[Interactive Discussion](#)


## Cloud top height trends in the oxygen A-band

L. Lelli et al.

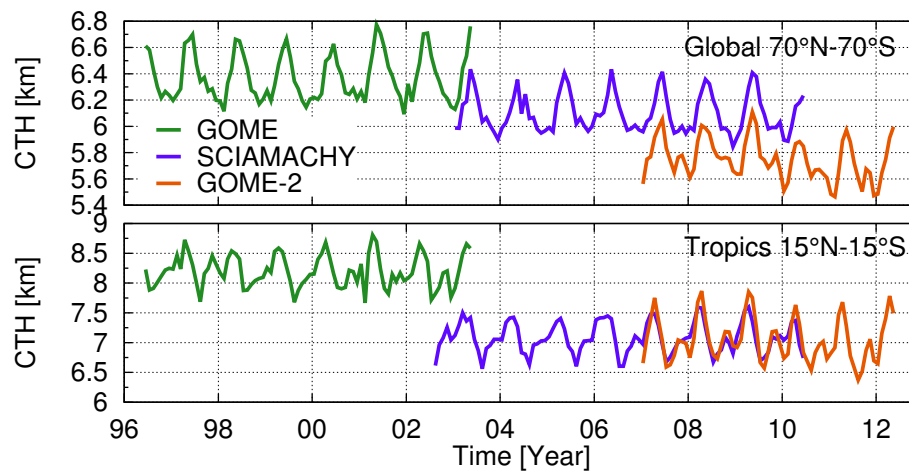


**Fig. 1.** Time series of monthly means of cloud top height for global (top) and tropical (bottom) region.

[Title Page](#)[Abstract](#)[Introduction](#)[Conclusions](#)[References](#)[Tables](#)[Figures](#)[⏪](#)[⏩](#)[◀](#)[▶](#)[Back](#)[Close](#)[Full Screen / Esc](#)[Printer-friendly Version](#)[Interactive Discussion](#)

## Cloud top height trends in the oxygen A-band

L. Lelli et al.

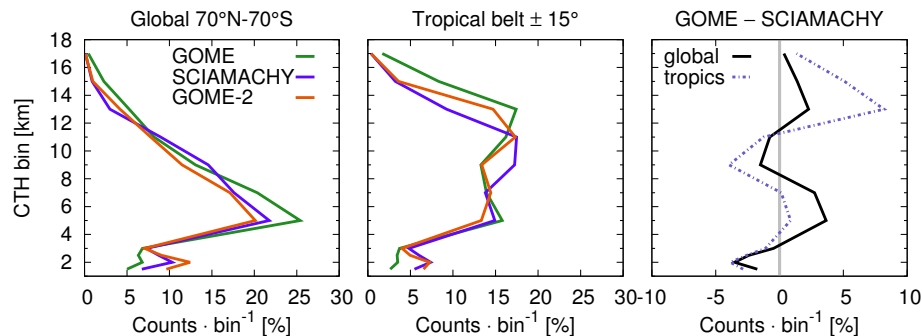


**Fig. 2.** Relative pixel count as function of height for different instruments for global (left) and tropical (mid) region. (Right) Count difference between GOME and SCIAMACHY. The coarse GOME footprint favors the detection of high clouds over low clouds.

## Cloud top height trends in the oxygen A-band

L. Lelli et al.

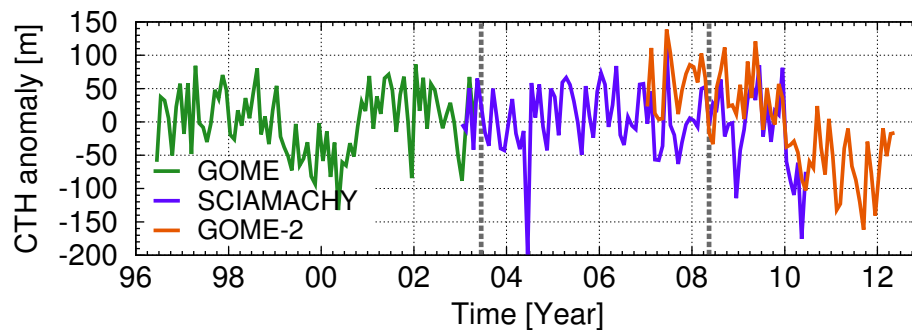


**Fig. 3.** Monthly means of cloud top height anomaly. The dashed gray vertical lines show the months at which the time series have been merged (June 2003 and May 2008).

[Title Page](#)[Abstract](#)[Introduction](#)[Conclusions](#)[References](#)[Tables](#)[Figures](#)[⏪](#)[⏩](#)[◀](#)[▶](#)[Back](#)[Close](#)[Full Screen / Esc](#)[Printer-friendly Version](#)[Interactive Discussion](#)

## Cloud top height trends in the oxygen A-band

L. Lelli et al.

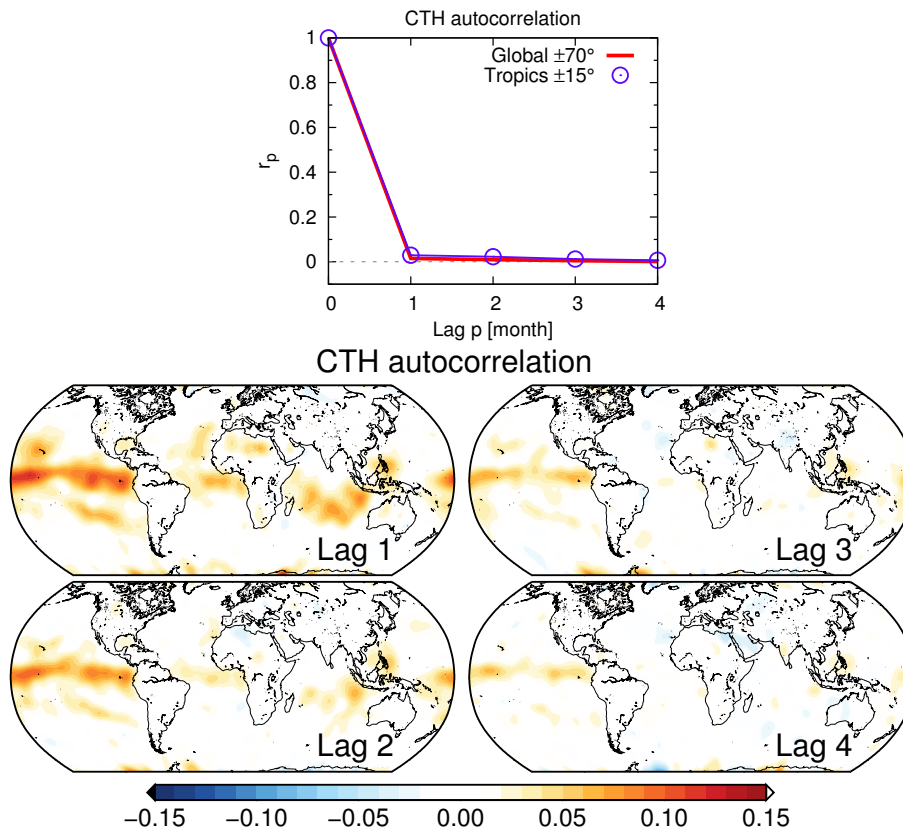


**Fig. 4.** (Upper plot) Autocorrelation function of cloud top height anomalies. Unlagged data ( $p = 0$ ) correlate perfectly with themselves ( $r_0 = 1$ ).  $r_p$  decays to almost 0 already at  $p = 1$ . (Lower plot) Maps of CTH autocorrelation for the first 4 months. ENSO-related patterns are seen over Pacific, Indian and Atlantic Oceans.

Title Page

Abstract

Introduction

Conclusions

References

Tables

Figures

◀

▶

◀

▶

Back

Close

Full Screen / Esc

Printer-friendly Version

Interactive Discussion

## Cloud top height trends in the oxygen A-band

L. Lelli et al.

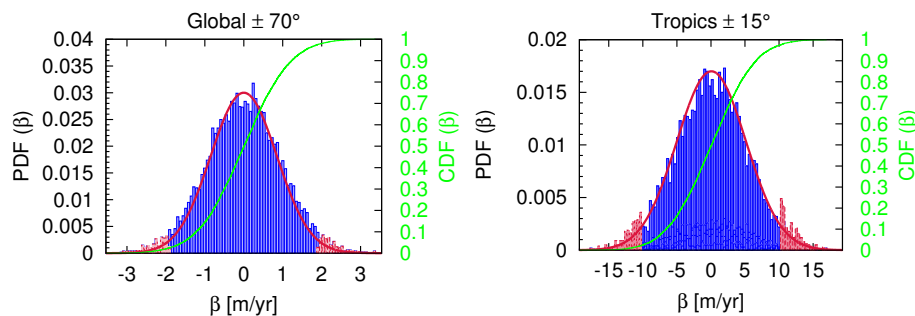


**Fig. 5.** Normalised bootstrap (resamples  $n = 10^4$ ) distributions of trend  $\beta$  for global (left) and tropical (right) regions. The red tails indicate the confidence interval (CI) at 95%. A Gaussian distribution and a cumulative distribution function are plotted in red and green, respectively.

[Title Page](#)[Abstract](#)[Introduction](#)[Conclusions](#)[References](#)[Tables](#)[Figures](#)[◀](#)[▶](#)[◀](#)[▶](#)[Back](#)[Close](#)[Full Screen / Esc](#)[Printer-friendly Version](#)[Interactive Discussion](#)

## Cloud top height trends in the oxygen A-band

L. Lelli et al.

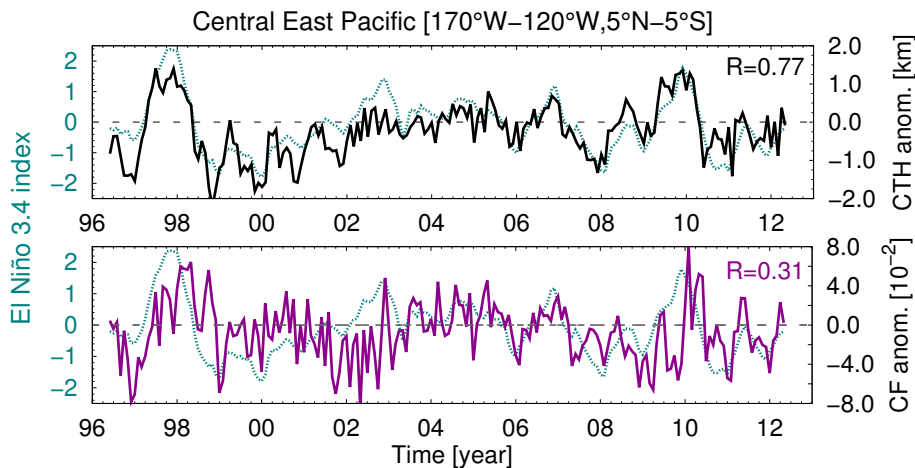


**Fig. 6.** Time series of cloud top height (top) and cloud fraction (bottom) anomaly over the Central East Pacific with the El Niño 3.4 index.

[Title Page](#)[Abstract](#)[Introduction](#)[Conclusions](#)[References](#)[Tables](#)[Figures](#)[◀](#)[▶](#)[◀](#)[▶](#)[Back](#)[Close](#)[Full Screen / Esc](#)[Printer-friendly Version](#)[Interactive Discussion](#)

## Cloud top height trends in the oxygen A-band

L. Lelli et al.

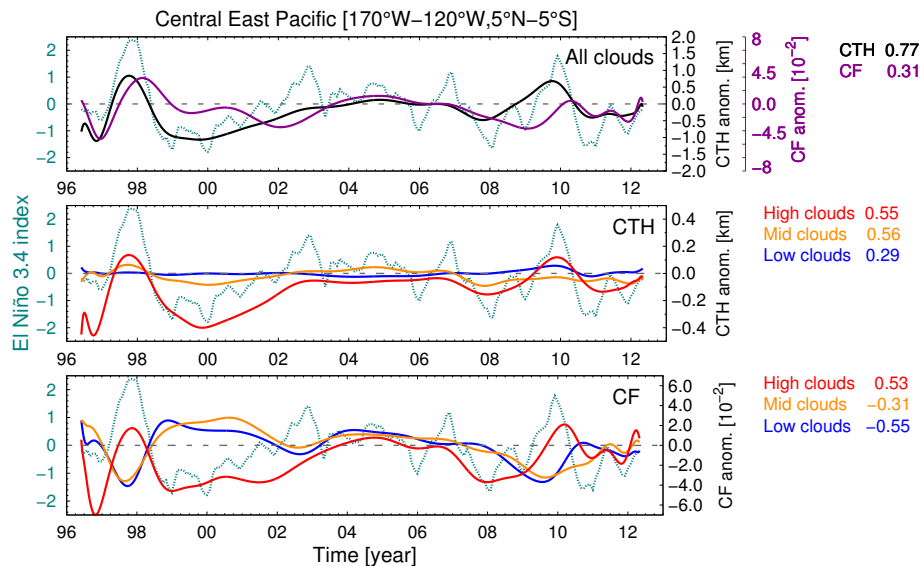


**Fig. 7.** (Top plot) Time series of cloud top height (black curve) and cloud fraction (purple) anomaly over the Central East Pacific with the El Niño 3.4 index and Pearson's correlation coefficient. (Mid plot) CTH and (bottom plot) CF anomalies subset for low- (blue), mid- (orange), and high-level (red) clouds. Time series smoothed with Bezier polynomials to increase readability. Correlation coefficients calculated with unsmoothed data.

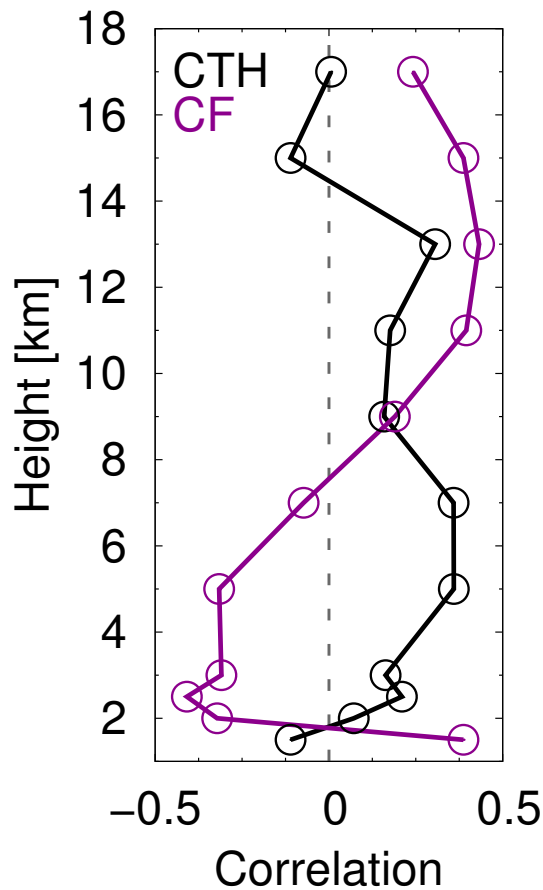


**Fig. 8.** Correlation coefficient of CTH and CF with the El Niño 3.4 index as function of height for the 17 yr of the GSG dataset.

**Cloud top height trends in the oxygen A-band**

L. Lelli et al.

Title Page

Abstract Introduction

Conclusions References

Tables Figures

◀ ▶

◀ ▶

Back Close

Full Screen / Esc

Printer-friendly Version

Interactive Discussion



## Cloud top height trends in the oxygen A-band

L. Lelli et al.

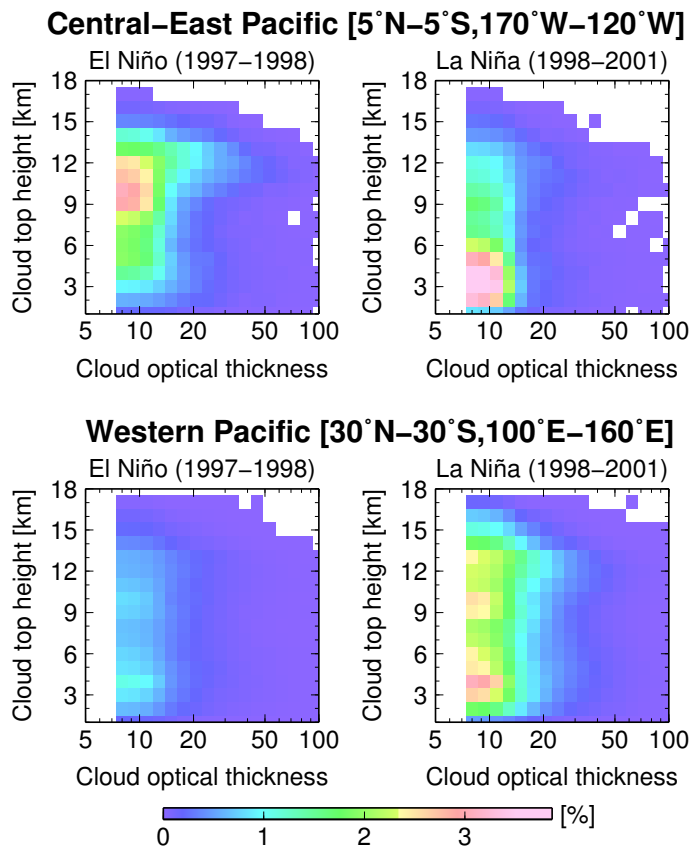


**Fig. 9.** ISCCP-like diagrams of cloud optical thickness vs. cloud top height for a warm (left column) and cold (right column) ENSO phase between April 1997 and June 2011 over the Niño 3.4 index box (top row) and the western tropical warm pool (bottom row).

## Cloud top height trends in the oxygen A-band

L. Lelli et al.

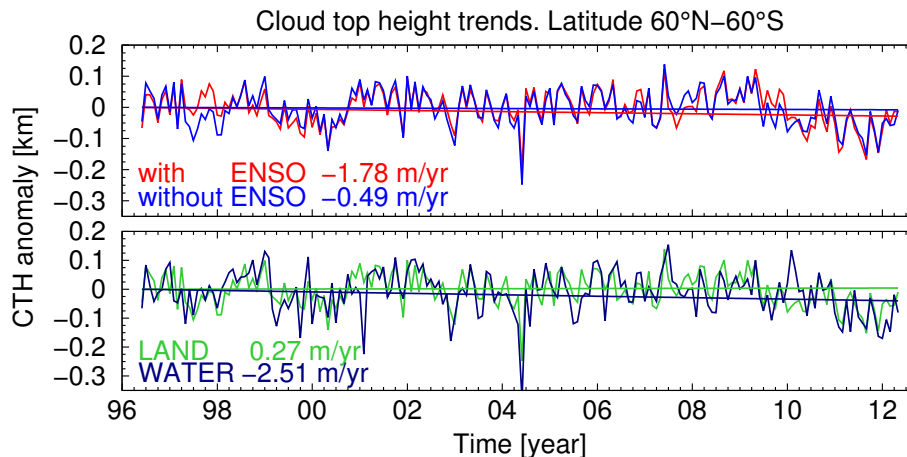


**Fig. 10.** (Upper plot) Global trend  $\beta$  in CTH anomalies in the latitude belt  $\pm 60^\circ$ , with (red line) and without (blue line) ENSO region. (Lower plot) The time series are broken up for underlying surface. Abundances of land and water masses between  $60^\circ$  N and  $60^\circ$  S are 0.264 and 0.736, respectively.

[Title Page](#)[Abstract](#)[Introduction](#)[Conclusions](#)[References](#)[Tables](#)[Figures](#)[◀](#)[▶](#)[◀](#)[▶](#)[Back](#)[Close](#)[Full Screen / Esc](#)[Printer-friendly Version](#)[Interactive Discussion](#)

## Cloud top height trends in the oxygen A-band

L. Lelli et al.

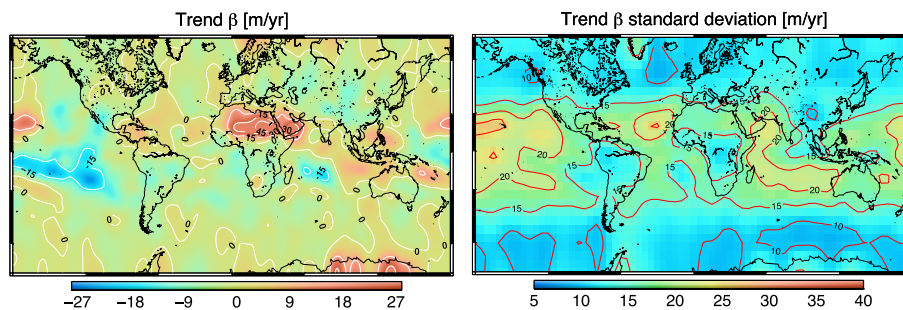


Fig. 11. Global map of linear trend  $\beta$  in CTH (left) and standard deviation  $\sigma_\beta$  (right).

Title Page

Abstract

Introduction

Conclusions

References

Tables

Figures

◀

▶

◀

▶

Back

Close

Full Screen / Esc

Printer-friendly Version

Interactive Discussion



## Cloud top height trends in the oxygen A-band

L. Lelli et al.

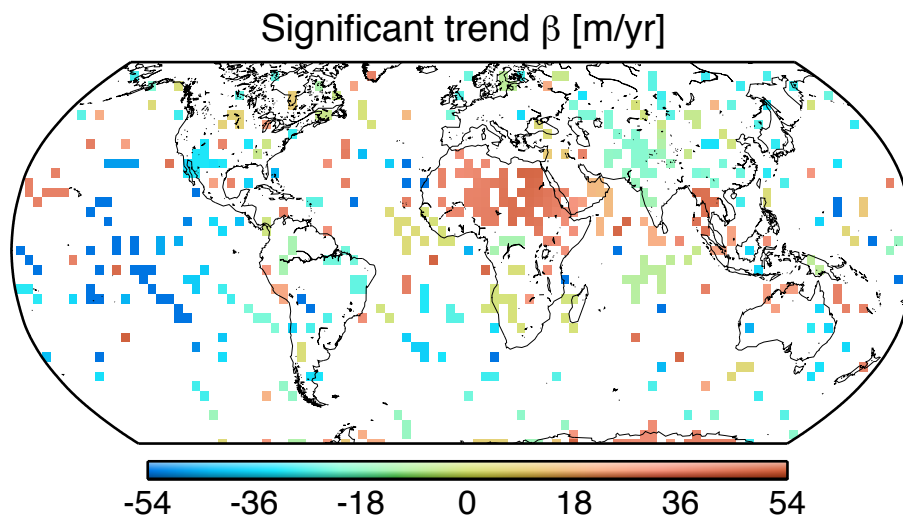


**Fig. 12.** Global trend  $\beta$  in CTH anomaly, statistically significant at 95 % confidence level. Data are gridded onto a mesh of  $2^\circ$ -sided cells.

[Title Page](#)[Abstract](#)[Introduction](#)[Conclusions](#)[References](#)[Tables](#)[Figures](#)[◀](#)[▶](#)[◀](#)[▶](#)[Back](#)[Close](#)[Full Screen / Esc](#)[Printer-friendly Version](#)[Interactive Discussion](#)

## Cloud top height trends in the oxygen A-band

L. Lelli et al.

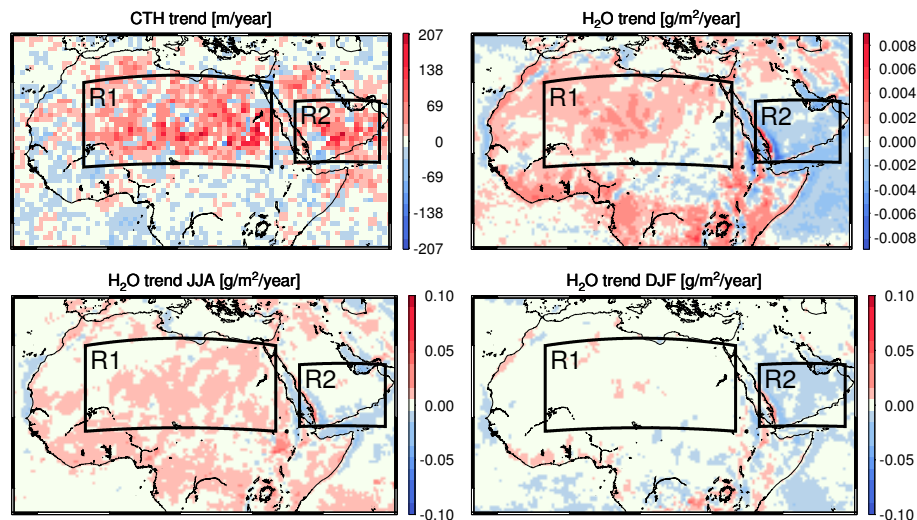


**Fig. 13.** Maps of linear trends over North Africa (R1) and Arabian Peninsula (R2) for (top left) CTH anomalies and (top right) columnar water vapor anomalies [ $\text{g m}^{-2} \text{yr}^{-1}$ ]. The latter is subset for (bottom left) summer (JJA) and (bottom right) winter (DJF) months.

[Title Page](#)[Abstract](#)[Introduction](#)[Conclusions](#)[References](#)[Tables](#)[Figures](#)[◀](#)[▶](#)[◀](#)[▶](#)[Back](#)[Close](#)[Full Screen / Esc](#)[Printer-friendly Version](#)[Interactive Discussion](#)